



## Research article

## Simulation and experimental validation of magnetic nanoparticle accumulation in a bloodstream mimicking flow system

Magdalena Reinelt<sup>a</sup>, Johannes Ahlfs<sup>b</sup>, Rene Stein<sup>b</sup>, Christoph Alexiou<sup>b</sup>, Eberhard Bänsch<sup>a</sup>, Ralf P. Friedrich<sup>b</sup>, Stefan Lyer<sup>b</sup>, Maria Neuss-Radu<sup>a</sup>, Nicolas Neuß<sup>a,\*</sup>

<sup>a</sup> Department of Mathematics, Friedrich-Alexander-Universität Erlangen-Nürnberg, Erlangen, Germany

<sup>b</sup> Department of Oto-Rhino-Laryngology, Head and Neck Surgery, Section of Experimental Oncology and Nanomedicine, Universitätsklinikum Erlangen, Germany

## ARTICLE INFO

## Keywords:

Magnetic drug targeting (MDT)  
Superparamagnetic nanoparticle (SPION)  
Magnetic force on nanoparticles  
Convection–diffusion equation  
Particle accumulation  
Finite element method (FEM)

## ABSTRACT

In this paper, a mathematical model for the dynamics of superparamagnetic iron oxide nanoparticles (SPIONs) in a laminar flow through a pipe under the influence of an external magnetic field of a single electromagnet is derived. The model consists of a convection–diffusion equation coupled with magnetostatic equations. The accumulation of particles along the boundary is modeled with the help of a surface concentration. Based on experimental data describing the retention of lauric acid coated SPIONs in a tubular flow under the influence of a magnetic field, the model is parametrized and finite element simulations are performed. With the exception of one outlier at low SPION concentration and high flowspeed, the simulation results agree very well with the experimental measurements within the bounds of the measurement error.

## 1. Introduction

Magnetic drug targeting (MDT) has been in the focus of researchers for decades, see e.g. [1]. The aim of the method is the precise application of pharmaceuticals to a diseased tissue or organ using magnetic nanocarriers that can be influenced in the body through an external magnetic field. As a result, the total amount of drug applied can be reduced, while increasing the therapeutic effect in the target area and reducing side effects. The importance of improving drug targeting can be exemplified by the fact that during a chemotherapy on average only 0.1% of drugs interact with tumorous cells. The remaining 99.9% ends up in healthy tissue causing huge damage [2]. Proposed fields of application are above all treatments of cancer and atherosclerosis.

Many investigations have been made in developing biocompatible nanoparticles that satisfy the demands for clinical use. Superparamagnetic iron oxide nanoparticles (SPIONs) with a size between 5 nm and 100 nm turned out to be the most promising base for further research on medical applications, including the development of a coating ensuring their stability in fluids and an incorporation of biochemical targeting molecules as well as the coupling with drugs [3]. In the treatment a suspension of primed particles is applied intra-arterially. Additionally, one or more external magnets have to be positioned such that a maximal dose accumulates in the desired tissue. In [4], it was shown that this can lead to a deposition of drug in the tumor area, which was up to 35 times

higher 24 h after the administration than the intravenous application of the unbound drug or the intravenous application of particle-bound drug with magnetic accumulation. In [5] experiments on a half-Y-branched glass tube model were performed and drug targeting maps, combining e.g. the magnetic volume force, the position of the magnet and the net amount of targeted nanoparticles were presented. In order to support the clinical use of MDT and to be able to offer a targeting efficiency tailored to each patient, mathematical models are needed to predict the targeting efficiency.

Many studies consider the mathematical modeling and the numerical simulation of MDT. E.g., in [6] by using Newton's second law trajectories of magnetic nanoparticles within a cylindrical vessel are determined analytically. Here, a linear magnetization model was used together with a laminar fluid flow profile. A further investigation using a particle-based approach is performed in [7], for the simulation of magnetic drug targeting in a multibranched vessel model. Mathematical models describing the evolution of the volumetric concentration of nanoparticles are considered, e.g., in [8] where a diffusion-advection for the nanoparticles is used together with a linear model for the magnetization and given flow profile. On the other hand, in [9,10] the transport equation for the nanoparticles are coupled to the Navier–Stokes equation for an incompressible viscous flow which contains

\* Corresponding author.

E-mail addresses: [reinelt@math.fau.de](mailto:reinelt@math.fau.de) (M. Reinelt), [johannes.ahlfs@uk-erlangen.de](mailto:johannes.ahlfs@uk-erlangen.de) (J. Ahlfs), [rene.stein@uk-erlangen.de](mailto:rene.stein@uk-erlangen.de) (R. Stein), [christoph.alexioiu@uk-erlangen.de](mailto:christoph.alexioiu@uk-erlangen.de) (C. Alexiou), [baensch@am.uni-erlangen.de](mailto:baensch@am.uni-erlangen.de) (E. Bänsch), [ralf.friedrich@uk-erlangen.de](mailto:ralf.friedrich@uk-erlangen.de) (R.P. Friedrich), [stefan.lyer@uk-erlangen.de](mailto:stefan.lyer@uk-erlangen.de) (S. Lyer), [maria.neuss-radu@math.fau.de](mailto:maria.neuss-radu@math.fau.de) (M. Neuss-Radu), [neuss@math.fau.de](mailto:neuss@math.fau.de) (N. Neuß).

<https://doi.org/10.1016/j.jmmm.2023.170984>

Received 19 January 2022; Received in revised form 26 May 2023; Accepted 28 June 2023

Available online 3 July 2023

0304-8853/© 2023 The Authors. Published by Elsevier B.V. This is an open access article under the CC BY license (<http://creativecommons.org/licenses/by/4.0/>).

## Nomenclature

<b>B</b>	Magnetic field, see Section 3.2
<b>B</b>	Magnitude of $p$ , see Section 3.2
<b>B<sub>e</sub></b>	External magnetic field, see Section 2.3
<b>c</b>	SPION volume fraction, see Section 2.2
<b>c<sub>b</sub></b>	SPIONs accumulated on $\partial\Omega$ , see Section 3.7
<b>c<sub>Fe</sub></b>	Iron concentration, see Section 2.2
<b>D</b>	SPION diffusion, see (28)
<b>F<sub>mag</sub></b>	Magnetic force, see Section 3.2
<b>F<sub>tot</sub></b>	Total force on a SPION, see Section 3.4
<b>H</b>	Magnetic field intensity, see Section 3.3
<b>J</b>	Flux of $c$ , see Section 3.6
<b>k<sub>B</sub></b>	Boltzmann constant, see Section 3.2
<b>L</b>	Langevin function, see Section 3.2
<b>m<sub>Fe</sub></b>	Injected iron mass, see Section 2.1
<b>m<sub>p</sub></b>	SPION particle mass, see Section 2.2
<b>m<sub>I</sub>, m<sub>S</sub></b>	Masses in $\Omega$ and on $\partial\Omega$ , see Section 3.9
<b>m<sub>T</sub></b>	Total mass, see Section 3.9
<b>M<sub>s</sub></b>	Saturation magnetization, see Eq. (16)
<b>P</b>	packing density factor, see Section 2.2
<b>Q</b>	Mean flux, see Section 2.1
<b>p</b>	SPION dipole moment, see Section 3.2
<b>p</b>	Magnitude of $p$ , see Section 2.2
<b>R<sub>p</sub></b>	SPION radius, see Section 2.2
<b>T<sub>K</sub></b>	Temperature in Kelvin, see Section 3.2
<b>V<sub>p</sub></b>	SPION volume, see Section 2.2

## Greek letters

<b>β</b>	SPION mobility, see Eq. (22)
<b>δ<sub>SD</sub></b>	SD parameter, see Section 4.1
<b>κ</b>	Aggregate size ratio, see Section 3.5
<b>μ<sub>0</sub></b>	Vacuum permeability, see Section 2.3
<b>ν</b>	Normal of $\partial\Omega$
<b>ξ</b>	Langevin parameter, see Eq. (9)
<b>Ω</b>	Model domain, see Section 3.1
<b>∂Ω</b>	Boundary of $\Omega$ , see Section 3.1
<b>∂Ω<sub>in</sub>, ∂Ω<sub>out</sub></b>	Inflow/outflow parts of $\partial\Omega$
<b>∂Ω<sub>lat</sub></b>	Lateral part of $\partial\Omega$

an additional magnetic volumetric force. First attempts to model the absorption of the nanoparticles into the blood vessel wall are done in [11] within a simplified two-dimensional geometrical setting. Membrane penetration of nanoparticles was considered e.g. in [12]. In [13] targeted drug delivery in a stenosed artery by using magnetic nanoparticles having an external influence of a magnetic field is modeled and simulated. And in [14], Shaw et al. introduce a model incorporating the rheology of real blood as well as the possibility of non-spherical porous particles. The model is evaluated by calculating the flow field analytically and afterwards particle trajectories numerically. In [15], the capture efficiency of carrier particles is studied numerically taking into account particle-particle interactions and the non-Newtonian behavior of real blood. In [16], a mathematical model for the dynamics of superparamagnetic nanoparticles under the influence of applied magnetic fields is derived. Here, the transport equation for the particle concentration and Maxwell's equations of magnetostatics are coupled via the particle magnetization. In two space dimensions, existence and uniqueness of a classical solution is proved in the radially symmetrical case.

This contribution treats both the modeling and the simulation of a basic MDT experiment, namely the accumulation of iron-oxide

nanoparticles in a blood stream mimicking phantom. The model consists of a diffusion-advection equation for the volume concentration of the nanoparticles coupled to Maxwell's equations of magnetostatics via the particle magnetization. Besides the magnetophoretic drift (induced by the magnetic force) the particles are advected by the background flow. Since the Reynolds number of the flow is rather small, the concentration of nanoparticles is low and the flow region consists of a straight tube with constant radius, the background flow is modeled as a Hagen–Poiseuille parabolic flow profile.

The retention of nanoparticles in the vessel is modeled as an accumulating surface concentration. Under simplifying assumptions in accordance with the experimental setting, numerical simulations are performed using a finite element approach. The computational methods are validated by numerical tests for mesh refinement, time step refinement, and the streamline diffusion method. Assuming the formation of SPION aggregates, see e.g., [17], the simulation results agree very well with the experimental measurements.

In contrast to previous work, this agreement is obtained using a relatively simple model. Furthermore, we carefully examine the dependence on various simulation parameters like mesh size, time step size, and stabilization parameters.

The paper is organized as follows: In Section 2, the experiment and its components is described in detail. Section 3 is concerned with the mathematical modeling of MDT both in general and in the particular situation of the experiment. Section 4 describes the numerical simulations of the simplified model and compares the simulation results with the experimental observations.

## 2. The magnetic drug targeting experiment

### 2.1. Experimental setup and results

The following experiment models the intraarterial injection of SPI-ONs (described in more detail in Section 2.2) and their targeting with a high gradient field electromagnet (described in more detail below in Section 2.3).

The setup is shown in Fig. 1. The measuring tubes with an inner diameter of 1.59 mm were cut into pieces of 53 cm each, and each end was connected to a vessel cannula and a conventional medical T-valve at each side. The accumulation tube (AT) was straightened with two clamps into a mounting. The inlet valve was connected to the supplying tube (ST) and the outlet valve to the collection tube (CT). The electromagnet was placed in the center of the mounting 6 mm above the AT. It was powered by a current of 72 A. The first section started at a reservoir with distilled water and ended in a peristaltic pump, where the mean flux  $Q$  was adjusted to 3.0 ml/min, 6 ml/min or 11 ml/min. The section starting at the pump ended in the inlet valve connected to the AT. A conventional intravenous catheter (IC) (22,5G) was inserted directly into the ST 20 cm before the inlet valve of the AT. A 1 ml-syringe filled with nanoparticle suspension without air bubbles was connected to the IC. In each experiment, a volume of 0.5 ml of nanoparticle suspension was applied at a iron concentration of 1 mg/ml, 2 mg/ml or 4 mg/ml over a time of 5 s. Hence, a total iron mass  $m_{Fe}$  of either 0.5 mg, 1 mg or 2 mg entered the tube system. After passing the accumulation area under the tip of the magnet, the liquid was collected in a 50 ml centrifuge tube until 4 min after the injection. The mass of collected SPIONs of each experiment was measured by AES (atomic emission spectroscopy), see [18], and the mass of retained particles in the AT was calculated by the difference of injected mass of iron and collected mass of iron in the centrifuge tube. Each data point consists of 16 single experiments which were measured in triplicates by AES. The percentage of retained particles is documented in Table 1 depending on the initial concentration and the flux.

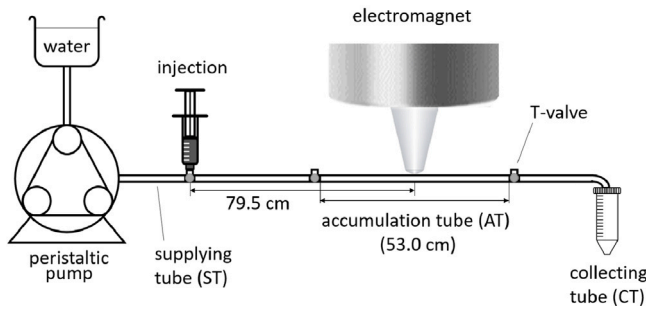


Fig. 1. Experimental setup. Water from the reservoir flows through the pump. Nanoparticles were injected 53 cm behind the pump and 79.5 cm in front of the magnet. The fluid was collected in a reservoir.

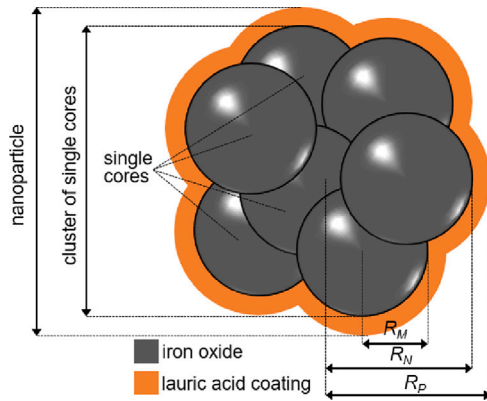


Fig. 2. Schematic and exemplary display of a single SPION. The nanoparticles used for the experiments were nanoclusters consisting of several single cores that were coated with a double layer of lauric acid.

Table 1

Retained percentage of the total injected iron mass with standard deviation at different fluxes and different initial suspension concentrations.

	Mean flux of peristaltic pump [ml/min]		
	3.0	6.0	11.0
Iron conc. [mg/ml]	1.0	2.0	4.0
	21.4 ± 4.1	27.6 ± 4.1	35.4 ± 4.0
	14.7 ± 5.3	13.3 ± 2.8	14.9 ± 4.3
	12.6 ± 3.7	8.7 ± 4.6	8.2 ± 6.1

## 2.2. Superparamagnetic iron-oxide nanoparticles (SPIONs)

In magnetic drug targeting, superparamagnetic iron-oxide nanoparticles (SPIONs) are used as vehicles for drug delivery, which can be directed into, or better accumulated in the diseased tissue by magnetic fields. These nanoparticles do not show any magnetic field as long as no external magnetic field is present. By this, the danger of unwanted accumulations and therefore thrombosis is minimized.

SPIONs consist of aggregations of multiple singlecores made up of maghemite ( $\text{Fe}_2\text{O}_3$ ) and magnetite ( $\text{Fe}_3\text{O}_4$ ) with a radius  $R_M = 5 \dots 9 \text{ nm}$ . The aggregation cluster has a radius of  $R_N = 59 \text{ nm}$ . To prevent further irreversible agglomeration of SPION, lauric acid is used to coat the surface of the clusters (see Fig. 2). With the lauric acid coating the radius of the final, coated SPION is  $R_P = 61 \text{ nm}$  (see Table 2). The volume of a coated particle is denoted by  $V_P$ . In the course of time the cluster oxidizes with a mass balance of 1 g of magnetite becoming 1.382 g of maghemite, such that the proportion of magnetite to maghemite and the mass of the cores changes. The outer layer is adjustable to the intended application, for example a composition of drug molecules and targeting-peptides may be used in context of magnetic drug targeting. In the experiments reported here no further coating was used.

Table 2

Size of particles used in this paper.

Particle type	Radius
Singlecores	$R_M \approx 7 \text{ nm} \pm 2 \text{ nm}$
Nanocluster	$R_N \approx 59 \text{ nm} \pm 1 \text{ nm}$
Iron-oxide nanoparticle (SPION)	$R_P \approx 61 \text{ nm} \pm 1 \text{ nm}$

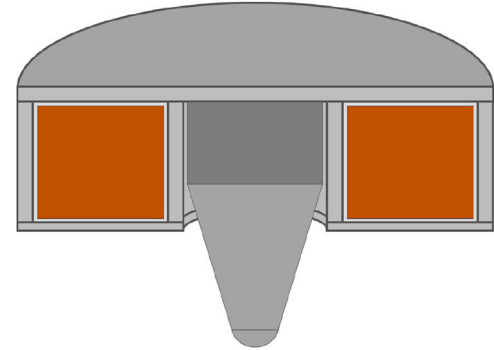


Fig. 3. Cross section of the Siemens electromagnet used in the experiment.

The mathematical analysis in Section 3 needs as further input the SPION mass  $m_P$  and the SPION dipole moment  $p$ . Assuming that both the nanoclusters and the SPIONs are approximately spherical, their volumes can be obtained as  $V_N = \frac{4}{3}\pi R_N^3 \approx 8.6 \times 10^{-22} \text{ m}^3$  and  $V_P = \frac{4}{3}\pi R_P^3 \approx 9.5 \times 10^{-22} \text{ m}^3$ , respectively, and an approximate mass of a SPION can then be obtained as

$$m_P = \rho_M P V_N + (V_P - V_N) \rho_L \approx 3.4 \cdot 10^{-18} \text{ kg} \quad (1)$$

using the density of magnetite/maghemite  $\rho_M \approx 5.2 \frac{\text{g}}{\text{cm}^3}$ , an assumed packing density  $P = 0.7405$  (spherical dense packing) of the singlecores inside the nanoclusters, and the density of lauric acid  $\rho_L \approx 1 \frac{\text{g}}{\text{cm}^3}$ .

The magnitude of the SPION dipole moment  $p$  can be calculated as

$$p = M_{\text{Mag}} P V_N \approx 2.9 \cdot 10^{-16} \text{ m}^2 \text{ A} \quad (2)$$

using the saturation magnetization of the magnetite/maghemite part of a SPION determined experimentally in [19]

$$M_{\text{Mag}} = \frac{1293 \text{ A/m}}{0.27\%} \approx 4.58 \cdot 10^5 \text{ A/m}. \quad (3)$$

Finally, let us denote by  $c$  the SPION volume fraction which is used in the mathematical model from Section 3. Then the iron concentration  $c_{\text{Fe}}$  (which is needed for calculating the mass of retained iron in Section 4) is related to  $c$  via

$$\frac{c_{\text{Fe}}}{c} = \frac{\text{SPION iron mass}}{\text{SPION volume}} = \frac{0.7 \cdot \rho_M P V_N}{V_P} \approx 2.44 \frac{\text{g}}{\text{cm}^3}$$

where a 70% iron mass fraction in maghemite/magnetite is assumed.

## 2.3. Electromagnet

The electromagnet used in the experiments is provided by Siemens AG Corporate Technologies, see [20]. As shown in Fig. 3, the core of the electromagnet consists of two parts: the inner part on which the windings are mounted and the cone-shaped outer part, which points to the target tissue. The outer part is geometrically designed in such a way that the magnetic field at the pole tip is as strong as possible in order to maximize the potential to enrich the nanoparticles in that area. It is made out of an iron-cobalt-alloy, which provides a remarkably high saturation magnetization of  $2.3 \text{ T}/\mu_0 \approx 1.83 \cdot 10^6 \text{ A/m}$ .

The electromagnet generates an inhomogeneous magnetic field  $B_e$ . Measurement of each component of  $B_e$  were taken by the manufacturer in a domain of  $5 \text{ cm} \times 10 \text{ cm} \times 10 \text{ cm}$  around the pole shoe. Inside that rectangular region a multilinear interpolation of these measurement

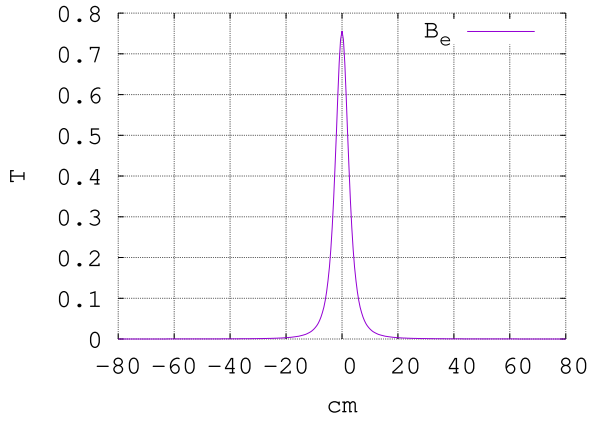


Fig. 4.  $B_e = |B_e|$  along the center line of the experimental tube.

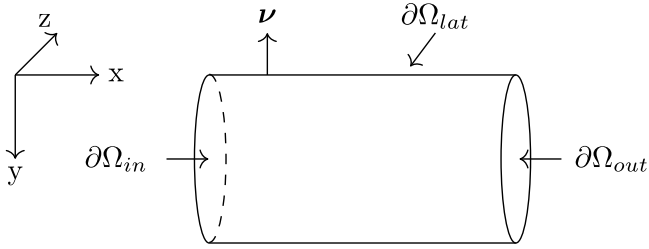


Fig. 5. A schematic domain  $\Omega$  with compartmentalized boundary  $\partial\Omega = \partial\Omega_{lat} \cup \partial\Omega_{in} \cup \partial\Omega_{out}$  and outer unit normal  $\mathbf{v}$ .

values was used. Outside of that region, the values were small and were approximated using a dipole field. The dipole strength and dipole position were obtained by a least-square fit of the measurement values.

$B_e = |B_e|$  is plotted in Fig. 4. Obviously, the magnetic field is very strong close to the pole shoe but decreases rapidly with increasing distance from it.

### 3. Mathematical modeling

#### 3.1. Computational domain

The pipe is modeled as a straight cylinder  $\overline{\Omega}$ , whose interior is denoted with  $\Omega$ . Its surface  $\partial\Omega = \overline{\Omega} \setminus \Omega$  is divided into three smooth parts: the lateral surface  $\partial\Omega_{lat}$ , the side of a net inflow of particles  $\partial\Omega_{in}$  and the side of the outflow of particles  $\partial\Omega_{out}$ . The complete boundary is denoted  $\partial\Omega := \partial\Omega_{lat} \cup \partial\Omega_{in} \cup \partial\Omega_{out}$  and its outer unit normal is denoted by  $\mathbf{v}$  (see Fig. 5).

#### 3.2. Magnetic force on SPIONs

Due to their small size SPIONs can be approximated as magnetic dipoles with magnetic dipole moments  $\mathbf{p}$ . It is assumed that their magnitude  $p := |\mathbf{p}|$  is constant (see (2)) and their orientation is random with a probability density dependent on the magnetic flux density.

Without an external magnetic field the average magnetic field of the particles arising from the dipole moments is zero. In the presence of an external magnetic field they orient themselves in direction of the field to a certain degree, resulting in a magnetization unequal to zero. This paramagnetic response of small ferrimagnetic dipoles is called superparamagnetic [21].

The force on a magnetic dipole is given as

$$\mathbf{F}_{\text{mag}} = \nabla(\mathbf{p} \cdot \mathbf{B}). \quad (4)$$

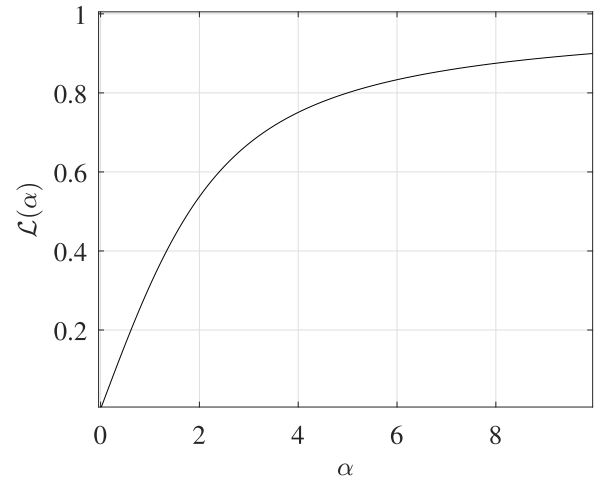


Fig. 6. The Langevin function  $\mathcal{L}(\alpha)$ .

(see e.g. [22]). Within this expression, the effective dipole-moment  $\mathbf{p}$  is given as the time-average

$$\mathbf{p} \approx p \overline{\cos \theta} \frac{\mathbf{B}}{B} \quad (5)$$

where  $B := |\mathbf{B}|$  and  $\theta$  is the angle between the dipole moment and the magnetic field. The distribution of  $\theta$  can be determined by using that the potential energy  $E_{\text{pot}}$  of the dipoles is given as (see [23])

$$E_{\text{pot}} = -\mathbf{p} \cdot \mathbf{B} = -pB \cos \theta \quad (6)$$

and that  $E_{\text{pot}}$  is distributed according to a Boltzmann distribution with density

$$f(E_{\text{pot}}) = \frac{e^{-E_{\text{pot}}/k_B T_K}}{\int_{-pB}^{+pB} e^{-E_{\text{pot}}/k_B T_K} dE_{\text{pot}}} \chi_{[-pB, pB]}, \quad (7)$$

where  $k_B$  is the Boltzmann constant,  $T_K$  the temperature measured in Kelvin, and  $\chi_{[-pB, pB]}$  the characteristic function of the interval  $[-pB, pB]$ . The expectation value  $\overline{\cos \theta}$  is then calculated by

$$\begin{aligned} \overline{\cos \theta} &= \int_{-1}^1 \cos \theta \frac{e^{pB \cos \theta / k_B T_K}}{\int_{-1}^1 e^{pB \cos \theta / k_B T_K} d \cos \theta} d \cos \theta \\ &= \coth \left( \frac{pB}{k_B T_K} \right) - \frac{k_B T_K}{pB} =: \mathcal{L} \left( \frac{pB}{k_B T_K} \right). \end{aligned} \quad (8)$$

The function  $\mathcal{L}(\alpha) = \coth(\alpha) - \frac{1}{\alpha}$ ,  $\alpha \in (0, \infty)$  is called the *Langevin function*, see Fig. 6.

Introducing

$$\xi := p/(k_B T_K) \approx 7.1 \times 10^4 \frac{\text{S}^2 \text{A}}{\text{kg}} \quad (9)$$

and using Eq. (8), Eq. (5) can be rewritten as

$$\mathbf{p} \approx p \mathcal{L}(\xi B) \frac{\mathbf{B}}{B}. \quad (10)$$

For weak magnetic flux densities with  $\xi B \ll 1$  the Langevin function can be approximated linearly by  $\mathcal{L}(\xi B) \approx \frac{1}{3} \xi B$  and for large arguments  $\xi B \gg 1$ , the approximation  $\mathcal{L}(\xi B) \approx 1 - (\xi B)^{-1}$  or even  $\mathcal{L}(\xi B) \approx 1$  is valid.

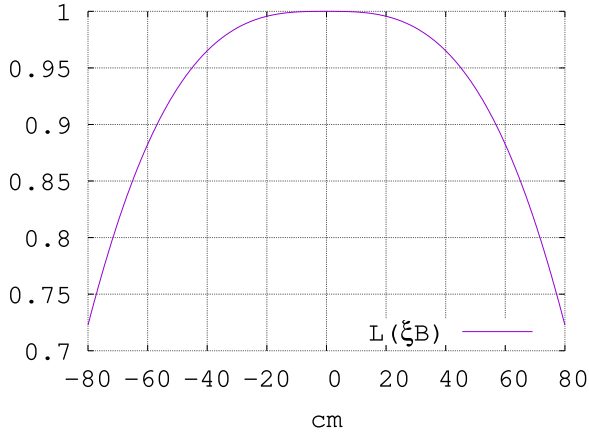
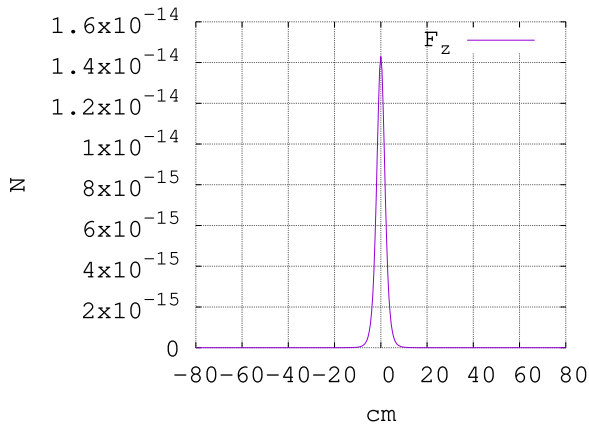
Neither of these approximations is appropriate in the whole domain, as can be seen from Fig. 7.

By inserting Eq. (10) into Eq. (4), the following expression for the force is obtained as

$$\mathbf{F}_{\text{mag}} = p \nabla \left( \mathcal{L}(\xi B) \mathbf{B} \cdot \frac{\mathbf{B}}{B} \right) = p \xi \tilde{\mathcal{L}}(\xi B) (\mathbf{B} \cdot \nabla) \mathbf{B}, \quad (11)$$

where  $\tilde{\mathcal{L}}(x) := \mathcal{L}'(x) + \frac{\mathcal{L}(x)}{x}$  was introduced as an abbreviation.

A plot of the vertical component of  $\mathbf{F}_{\text{mag}}$  along the experimental tube using  $\mathbf{B} = \mathbf{B}_e$  from Section 2.3 is shown in Fig. 8.

Fig. 7.  $L(\xi B)$  along the center line of the experimental tube.Fig. 8. Vertical component of  $F_{\text{mag}}$  along the center line of the experimental tube.

### 3.3. Magnetostatic equations

According to [24], a quasi-static magnetic field is described by the stationary Maxwell equations

$$\nabla \times \mathbf{H} = \mathbf{j}, \quad (12)$$

$$\nabla \cdot \mathbf{B} = 0, \quad (13)$$

with the magnetic flux density  $\mathbf{B}$ , the magnetic field intensity  $\mathbf{H}$  and the electric current density  $\mathbf{j}$ . The material dependent constitutive equation can be written as

$$\mathbf{B} = \mu \mathbf{H} = \mu_0 (\mathbf{H} + \mathbf{M}), \quad (14)$$

with the vacuum permeability  $\mu_0$ , the material-dependent magnetic permeability  $\mu$ , and the magnetization  $\mathbf{M}$ . Note that in general  $\mu$  and  $\mathbf{M}$  are nonlinear functions of  $\mathbf{B}$ , such that Eq. (14) is rather an implicit relation with respect to  $\mathbf{B}$ .

The magnetization of a single SPION with volume  $V_p$  is given as

$$\mathbf{M}_p = \frac{\mathbf{p}}{V_p}, \quad (15)$$

which is a vectorial quantity and its absolute value (the scalar saturation magnetization) can be calculated using Eq. (2) as

$$M_s = \frac{p}{V_p} \approx 3.07 \times 10^5 \frac{\text{A}}{\text{m}}. \quad (16)$$

Replacing  $p$  in Eq. (15) by its approximation Eq. (10) leads to

$$\mathbf{M}_p = \frac{p}{V_p} \mathcal{L}(\xi B) \frac{\mathbf{B}}{B} = M_s \mathcal{L}(\xi B) \frac{\mathbf{B}}{B}. \quad (17)$$

For a suspension of magnetic particles, the local average magnetization of the particles and the surrounding medium is considered. As the magnetization of distilled water is very small, it is set to zero in the following. The average magnetization is given by the volume fraction  $c$  of the SPIONs times the magnetization of a particle, that is

$$\mathbf{M} = c \mathbf{M}_p = c M_s \mathcal{L}(\xi B) \frac{\mathbf{B}}{B}. \quad (18)$$

Finally, using Eq. (14) leads to the following implicit formula for  $\mathbf{B}$ :

$$\mathbf{B} = \mu_0 \mathbf{H} + \left( \mu_0 c M_s \mathcal{L}(\xi B) \frac{\mathbf{B}}{B} \right). \quad (19)$$

### 3.4. Forces and induced flow field

Two kinds of forces acting on SPION particles of radius  $R_p$  are relevant here, namely the magnetic force  $\mathbf{F}_{\text{mag}}$  and the gravitational force  $\mathbf{F}_{\text{grav}}$ . The magnetic force  $\mathbf{F}_{\text{mag}}$  is given by Eq. (11), and the latter is given as

$$\mathbf{F}_{\text{grav}} = V_p \delta \rho \mathbf{g} = (m_p - V_p \rho_{\text{H}_2\text{O}}) \mathbf{g} \quad (20)$$

where  $\mathbf{g}$  is the gravitational acceleration vector,  $\delta \rho = \rho_p - \rho_{\text{H}_2\text{O}}$  denotes the difference between SPION density and water density, and  $V_p$  is the SPION volume. Note that  $\mathbf{F}_{\text{grav}}$  is an effective gravitational force (also called hydrostatic weight).

The total force (per particle)

$$\mathbf{F}_{\text{tot}} = \mathbf{F}_{\text{mag}} + \mathbf{F}_{\text{grav}} \quad (21)$$

then causes an acceleration of particles in direction of the force. As the movement of these particles takes place relative to a background flow field  $\mathbf{v}_0$  in a liquid with viscosity  $\eta$ , the friction force is calculated by Stokes' law (see [25])

$$\mathbf{F}_{\text{fric}} = -6\pi\eta R_p (\mathbf{v} - \mathbf{v}_0) = -\frac{1}{\beta} (\mathbf{v} - \mathbf{v}_0),$$

where  $\mathbf{v}_0$  is given by the laminar fluid flow profile and

$$\beta = \frac{1}{6\pi\eta R_p} \approx 8.7 \times 10^8 \frac{\text{s}}{\text{kg}} \quad (22)$$

is the particle mobility.

Then the particle velocity at the balance of forces  $\mathbf{F}_{\text{tot}} + \mathbf{F}_{\text{fric}} = \mathbf{0}$  is given by

$$\mathbf{v} = \mathbf{v}_0 + \beta \mathbf{F}_{\text{tot}}. \quad (23)$$

Obviously, the gravitational force from Eq. (20) is constant along the tube, and its magnitude can be computed using (20)

$$F_{\text{grav}} = (m_p - \rho_{\text{H}_2\text{O}} V_p) g = 2.4 \times 10^{-17} \text{ N}. \quad (24)$$

Thus,  $F_{\text{grav}}$  is up to three orders of magnitude smaller than the contributions due to  $F_{\text{mag}}$  near the pole-tip (see Fig. 8), but dominates when the distance from the pole-tip is larger than about 10 cm.

### 3.5. SPION aggregation

Calculating the particle drift velocity  $\mathbf{v}$  from Eq. (23) using  $\mathbf{F}_{\text{mag}}$  from Fig. 8 leads to the graph shown in Fig. 9. This drift would be much too small to account for the particle accumulation observed in Section 2, Table 1. The same phenomenon was also reported in [21, 26] where much larger velocities than expected were observed. A reasonable explanation for this difference is the formation of particle aggregates. This has been confirmed, e.g., by [17], where the formation of chain-like aggregates is observed and [27] where the magnetophoretically induced velocity was measured as function of particles in the chain-like aggregates.

Since it is far too difficult to model the formation process and the possible geometries of such aggregates at the moment, the following analysis assumes spherical aggregates of the same size which are made up by packing SPIONs with a packing density  $P = 0.74$  (dense packing of spheres).



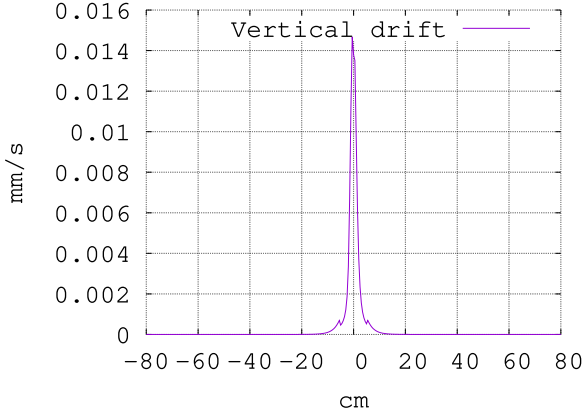


Fig. 9. Vertical drift velocity along the center line of the experimental tube.

Let  $n$  be the average number of particles in such an aggregate with radius  $R$  and  $P$  the packing density as above. Introducing the relative aggregate size as the ratio  $\kappa := R/R_p$  and indexing quantities referring to aggregates with  $R$ , one obtains for spherical aggregates approximately

$$V_R = \frac{nV_p}{P}, \quad n = P \frac{V_R}{V_p} = P\kappa^3.$$

Now, the total force on such an aggregate is  $n$ -times the force on a single particle, whereas the mobility is given by

$$\beta_R := \frac{1}{6\pi\eta R} = \frac{1}{\kappa} \beta.$$

In consequence, the drift velocity is enhanced by a factor  $P\kappa^2$  for SPION aggregates of relative size  $\kappa$ , such that Eq. (23) becomes

$$\mathbf{v} = \mathbf{v}_0 + P\kappa^2 \beta \mathbf{F}_{\text{tot}}. \quad (25)$$

### 3.6. Transport equation

The SPION volume fraction  $c$  satisfies a convection–diffusion equation

$$\frac{\partial c}{\partial t} + \nabla \cdot \mathbf{J} = 0 \quad (26)$$

with the flux  $\mathbf{J}$ . This flux consists of a convective part

$$\mathbf{J}_{\text{conv}} = c\mathbf{v} \quad (27)$$

with  $\mathbf{v}$  from Eq. (25) and a diffusive part (see [28])

$$\mathbf{J}_D = -D\nabla c, \quad D = \frac{k_B T_K}{6\pi\eta R_p}, \quad (28)$$

where  $R_p$  is the particle radius from Section 2.2.

The total flux of particles is then given as the sum of the fluxes resulting in

$$\mathbf{J} = -D\nabla c + c\mathbf{v} \quad (29)$$

such that the transport equation reads

$$\partial_t c + \nabla \cdot (-D\nabla c + c\mathbf{v}) = 0. \quad (30)$$

with  $\mathbf{v} = \mathbf{v}(\mathbf{B})$  from Eq. (25) and  $D$  from Eq. (28).

Note that this equation is valid only for small SPION concentrations  $c < 1$ , and that it cannot hold in the case  $c \approx 1$ , because then the influence of the moving particles on the flow  $\mathbf{v}_0$  cannot be neglected.

### 3.7. Boundary conditions

The inflow of particles at  $\partial\Omega_{in}$  is modeled with a Neumann boundary condition corresponding to a time-varying flux of the form

$$\mathbf{J} \cdot \mathbf{v} = -c_{in}(t) \mathbf{v}_0 \cdot \mathbf{v} \quad \text{on } \partial\Omega_{in} \times (0, T), \quad (31)$$

while at  $\partial\Omega_{out}$  the outflow condition

$$\mathbf{J} \cdot \mathbf{v} = c \mathbf{v}_0 \cdot \mathbf{v} \quad \text{on } \partial\Omega_{out} \times (0, T). \quad (32)$$

On  $\partial\Omega_{lat}$  particles can accumulate according to

$$\frac{\partial c_b}{\partial t} = \mathbf{J} \cdot \mathbf{v} \quad \text{on } \partial\Omega_{lat}, \quad (33)$$

$$\mathbf{J} \cdot \mathbf{v} = c \mathbf{v} \cdot \mathbf{v} \quad \text{on } \partial\Omega_{lat}. \quad (34)$$

Here,  $c_b$  is a function defined only on the lateral boundary which models particles accumulating at the surface of the pipe. Its unit is mm, corresponding to the thickness of the accumulated particle film, and its integration over the whole surface  $\partial\Omega$  results in a volume which can be identified with a certain mass.

Obviously, also  $c_b$  has to remain small, because otherwise the influence on the flow field  $\mathbf{v}_0$  cannot be neglected.

### 3.8. Full model

Since  $\mathbf{H}$  is curl-free in  $\Omega$ ,  $\mathbf{H}$  can be expressed using its potential  $\Phi$  as

$$\mathbf{H} = \nabla \Phi. \quad (35)$$

Then Eq. (12) is always fulfilled (with  $j = 0$ ) and the system of equations reduces to Eqs. (13) and (19).

Let  $\Omega$  denote the domain from Section 3.1 and let  $T > 0$  denote the end time of the simulation. Then the following three partial differential equations have to be solved in  $\Omega \times (0, T)$ :

$$\nabla \cdot \mathbf{B} = 0, \quad (36)$$

$$\mathbf{B} = \mu_0 \nabla \Phi + \left( \mu_0 c M_s \mathcal{L} \left( \xi \mathbf{B} \right) \frac{\mathbf{B}}{B} \right), \quad (37)$$

$$\partial_t c + \nabla \cdot \left( -D\nabla c + \mathbf{v}_0 c + \beta p c \xi \tilde{\mathcal{L}} \left( \xi \mathbf{B} \right) (\mathbf{B} \cdot \nabla) \mathbf{B} \right) = 0. \quad (38)$$

The boundary conditions for  $c$  are given by Eqs. (31)–(34). Initially, both  $c$  and also the boundary concentration  $c_b$  are set to zero at the initial time

$$c(x, 0) = 0 \quad \text{in } \Omega \times \{0\}, \quad (39)$$

$$c_b(x, 0) = 0 \quad \text{in } \partial\Omega_{lat} \times \{0\}. \quad (40)$$

Boundary conditions for the potential  $\Phi$  are obtained by assuming that the exterior magnetic field is not changed much due to the processes in the tube. Then, the normal components the magnetic flux density must satisfy

$$\mathbf{v} \cdot (\mathbf{B} - \mathbf{B}_e) = 0 \quad \text{on } \partial\Omega \quad (41)$$

where  $\mathbf{B}_e$  denotes the magnetic flux density outside of  $\Omega$ .

### 3.9. Simplified model

Based on the special features of our experimental setting, the model from Section 3.8 can be simplified as follows. First, in the model above the magnetization of the fluid influences the magnetic flux. If one neglects this influence, one may approximate the magnetic flux density by  $\mu_0 \mathbf{H}$ , as it was done in e.g. [29,30]. This does not yield adequate results in every scenario, as is shown for example by measurements presented in [31]. However, in the case of small particle concentration, the magnetization is small as well and the equations decouple. It

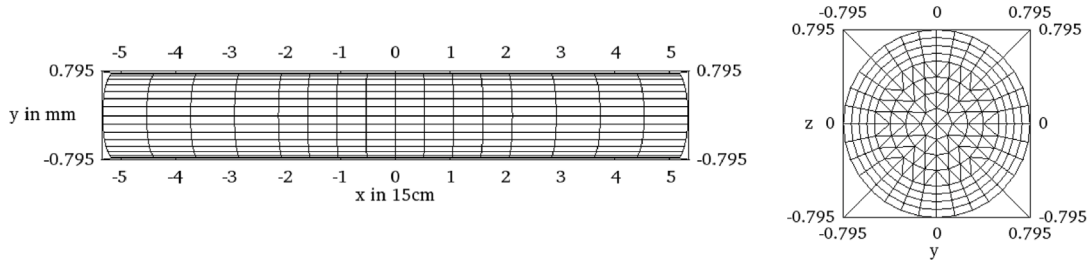


Fig. 10. Lateral and radial view on the mesh. The  $x$ -axis is scaled by a factor of  $1/150$ , such that its labels are given in units of  $15\text{ cm}$ , while the  $z$ - and  $y$ -axis are labeled in  $\text{mm}$ .

follows that the magnetic field is static and can be determined either by measurements or by performing a separate calculation for the given configuration. Second, gravity effects on the particles are much smaller than the magnetic effects and can be neglected (see the discussion at the end of Section 3.4).

Based on these simplifications the model reduces to the following partial differential equation

$$\partial_t c + \nabla \cdot \left( -D \nabla c + \mathbf{v}_0 c + P \kappa^2 \beta p c \xi \tilde{\mathcal{L}}(\xi \mathbf{B})(\mathbf{B} \cdot \nabla) \mathbf{B} \right) = 0 \quad (42)$$

in  $\Omega$  with the following initial and boundary conditions

$$\mathbf{J} \cdot \mathbf{v} = -c_{in}(t) \mathbf{v}_0 \cdot \mathbf{v} \quad \text{on } \partial\Omega_{in} \times (0, T), \quad (43)$$

$$\mathbf{J} \cdot \mathbf{v} = c \mathbf{v}_0 \cdot \mathbf{v} \quad \text{on } \partial\Omega_{out} \times (0, T), \quad (44)$$

$$\frac{\partial c_b}{\partial t} = \mathbf{J} \cdot \mathbf{v} \quad \text{on } \partial\Omega_{lat}, \quad (45)$$

$$\mathbf{J} \cdot \mathbf{v} = P \kappa^2 \beta F_{mag} c \cdot \mathbf{v} \quad \text{on } \partial\Omega_{lat}, \quad (46)$$

$$c(x, 0) = 0 \quad \text{in } \Omega \times \{0\}, \quad (47)$$

$$c_b(x, 0) = 0 \quad \text{in } \partial\Omega \times \{0\}. \quad (48)$$

Finally, the following integrated quantities will be used in the following section:

$$m_I(t) := \int_{\Omega} c(x, t) dx, \quad (49)$$

$$m_S(t) := \int_{\partial\Omega} c_b(x, t) dx, \quad (50)$$

$$m_T(t) := m_I(t) + m_S(t). \quad (51)$$

Here,  $m_I$  describes the particle content in  $\Omega$ ,  $m_S$  in the surface aggregate, and the total mass  $m_T$  is the sum of both.

## 4. Numerical simulations

### 4.1. Numerical methods

Simulations of the model described in Section 3.9 are performed in the open source Common Lisp framework FEMLISP developed by N. Neuß [32,33].

The time discretization of the system consisting of Eq. (38) and Eqs. (33), (34) is done with Rothe's method (which is an implicit Euler method in time). Let  $0 = t_0, t_1, \dots, t_{N_T} = T$  be points in time with time step size  $\Delta t_n = t_n - t_{n-1}$  for  $n = 1, \dots, N_T$ . Denoting  $c^n := c(\cdot, t_n)$ ,  $c_b^n := c_b(\cdot, t_n)$ , the following system of linear partial differential equations has to be solved for obtaining  $(c^n, c_b^n)$  from  $(c^{n-1}, c_b^{n-1})$ :

For  $n = 1, \dots, N_T$ :

$$\text{In } \Omega : \frac{c^n}{\Delta t_n} + \nabla \cdot \left( -\nabla c^n + \mathbf{v}_0 c^n + P \kappa^2 \beta p c^n \xi \tilde{\mathcal{L}}(\xi \mathbf{B})(\mathbf{B} \cdot \nabla) \mathbf{B} \right) = \frac{c^{n-1}}{\Delta t_n}, \quad (52)$$

$$\text{On } \partial\Omega_{lat} : \frac{c_b^n}{\Delta t_n} = \frac{c_b^{n-1}}{\Delta t_n} + \beta F_{mag} c^{n-1}. \quad (53)$$

The time step size  $\Delta t_n$  influences the accuracy of the method. A suitable value will be determined experimentally in the next section. In principle,  $\Delta t_n$  could be changed from step to step using adaptive time-stepping strategies. For simplicity, we use a constant time step  $\Delta t$ , i.e.  $\Delta t_n = \Delta t = \frac{T}{N_T}$  for all  $n = 1, \dots, N_T$ .

The space discretization is performed with the finite element (FE) method on non-uniform meshes  $\mathcal{E}_k$ ,  $k = 1, 2, 3$  (see Fig. 10, which shows  $\mathcal{E}_2$ ). These meshes consists of curvilinear hexahedra, prisms and bent rectangles and the FE basis functions are set to be trilinear (for  $c$ ) respectively bilinear (for  $c_b$ ) on the reference cells. For  $k = 1, 2$ ,  $\mathcal{E}_{k+1}$  is obtained from  $\mathcal{E}_k$  by uniform refinement.

Without stabilization the spatial discretization suffers from typical instabilities due to the dominant convection term in the convection-diffusion equation for the concentration, resulting in a global Péclet number larger than  $3.4 \cdot 10^7$ . Therefore, it is stabilized using a reduced streamline diffusion method which adds an artificial anisotropic diffusion of the form

$$\delta_{SD} \sum_{E \in \mathcal{E}} \int_E \left( \frac{\mathbf{v} \mathbf{v}^T}{2\hat{v}} \nabla c_h^n \right) \cdot \nabla \varphi_h,$$

to Eq. (38). Here,  $\delta_{SD}$  is a scaling parameter,  $c_h^n$  is the time and space discretized solution,  $\varphi_h$  is the FE test function and  $\hat{v}$  is the magnitude of the velocity  $\mathbf{v}$  on the reference element. Due to the transformation between global and local coordinates, the ratio of  $v$  to  $\hat{v}$  is mesh-dependent.

Application of the FE method in the Galerkin way (i.e. the test space is the same as the ansatz space) and choosing a basis for the ansatz space (we use a Lagrange basis where the node functionals are the values at the mesh vertices), transforms the differential equations (52), (53) into a linear system of algebraic equations. This linear algebraic system is then solved using the biconjugate gradient stabilized method (BiCGStab, [34]). The stopping criterion of the BiCGStab iteration was chosen such that the vector of residues is smaller than  $10^{-10}$ .

### 4.2. Validation of the computational method

In this part numerical tests of mesh refinement, time step refinement, and the streamline diffusion method are presented. In every case, the accumulated masses  $m_I, m_S, m_T$  defined in (49), (50), (51) are compared.

First, the influence of mesh refinement is examined. The base mesh consists of 480 cells and is referred to as 'level 1' mesh. This mesh is then refined uniformly resulting in a 'level 2' mesh consisting of 3840 cells (see Fig. 10), and a further uniform refinement leads to a 'level 3' mesh consisting of 30720 cells. Fig. 11 shows the masses  $m_I$  and  $m_S$  computed with these meshes as functions of the model time, where parameters were set to  $Q = 6\text{ ml/min}$ ,  $\kappa = 5$  (which is a reasonable value, see the tests below),  $\delta_{SD} = 0.5$  and a total inflow of  $2\text{ mg}$  iron. The simulation on the coarsest mesh leads to a significantly lower mass of retained particles but the level 2 and level 3 simulations coincide well, which allows us to continue with the level 2 mesh. Retained iron mass (in percent of the total injected iron mass) at time  $120\text{ s}$  are listed in Table 3. The level 3 simulation shows that  $17.43\%$  of particles are

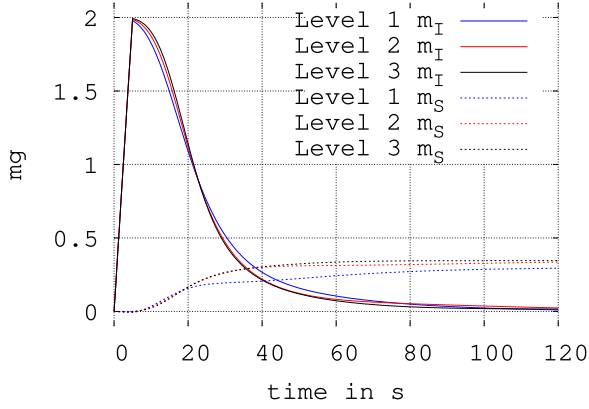


Fig. 11. Masses  $m_I$  of particles inside  $\Omega$  and masses  $m_S$  accumulated on  $\partial\Omega$  for simulations on three different meshes.

Table 3

Retained percentage of the total injected iron mass (on the surface ( $m_S$ ), in the interior ( $m_I$ ), and total ( $m_T$ )) after 2 min for different levels of refinement. Parameters for the simulation are set to  $\kappa = 5$ ,  $Q = 6$  ml/min,  $\Delta t = 0.5$  s,  $\delta_{SD} = 0.5$  and a total inflow of 2 mg iron.

	Refinement level		
	1	2	3
$m_S(120\text{ s})$	14.71	16.79	17.31
$m_I(120\text{ s})$	0.55	1.20	0.82
$m_T(120\text{ s})$	15.26	17.99	18.13

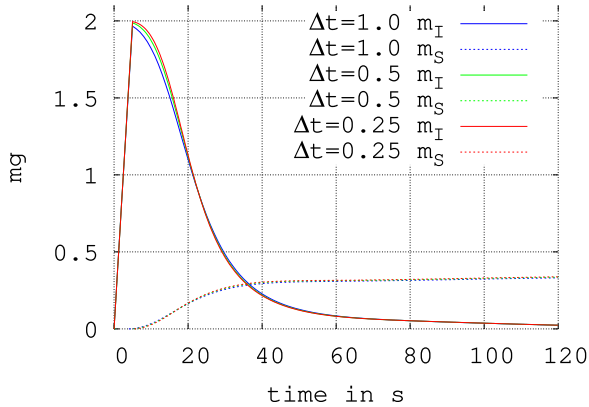


Fig. 12. Masses  $m_I$  of particles inside  $\Omega$  and masses  $m_S$  of the accumulated nanoparticles on  $\partial\Omega$  for simulations with different time step sizes  $\Delta t$ .

retained compared with 16.91% on the level 2 mesh which means that the relative error on level 2 is about 3%.

Next the influence of the time step size is investigated. Parameters are chosen as above, except for  $\delta_{SD} = 0.3$  which is a little lower. The solutions for  $\Delta t = 0.25$  s,  $\Delta t = 0.5$  s, and  $\Delta t = 1.0$  s are shown in Fig. 12 by means of the mass of particles during the simulation. One can see that the curves look almost identical. Some values at the end time 120 s are listed in Table 4, from where one can see that a choice of time step of  $\Delta t = 0.5$  s leads to an error of about 1%–2% in total quantities.

The last numerical test deals with the streamline diffusion scaling parameter  $\delta_{SD}$ . Simulations were performed with varying  $\delta_{SD}$  for a mean flux of  $Q = 6$  ml/min,  $\Delta t = 0.5$  s and remaining parameters as above. Fig. 13 shows particles masses as a function of time for

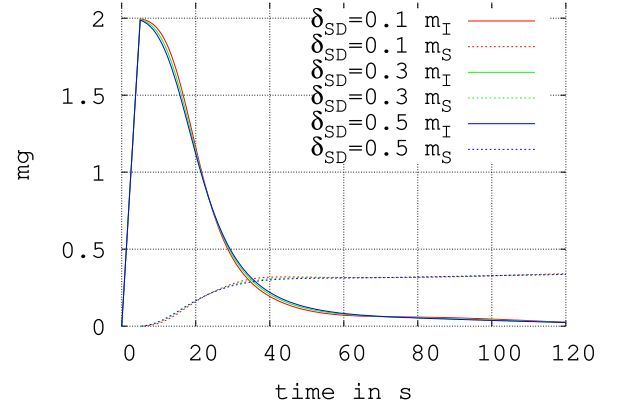


Fig. 13. Masses  $m_I$  of particles inside  $\Omega$  and masses  $m_S$  accumulated on  $\partial\Omega$  for simulations with different streamline diffusion parameters. Parameters are set to  $Q = 6$  ml/min and a total inflow of 2 mg iron.

Table 4

Retained percentage of the total injected iron mass (on the surface ( $m_S$ ), in the interior ( $m_I$ ), and total ( $m_T$ )) after 2 min for different time step sizes and parameters  $Q = 6$  ml/min and a total inflow of 2 mg iron.

	Time step size $\Delta t_n$ [s]				
	0.25	0.5	1.0	2.0	4.0
$m_S(120\text{ s})$	16.91	16.79	16.57	16.26	15.73
$m_I(120\text{ s})$	1.20	1.20	1.20	1.18	1.19
$m_T(120\text{ s})$	18.11	17.99	17.77	17.44	16.91

Table 5

Retained percentage of the total injected iron mass (on the surface ( $m_S$ ), in the interior ( $m_I$ ), and total ( $m_T$ )) after 2 min for different streamline diffusion parameters and  $Q = 6$  ml/min and a total inflow of 2 mg iron.

	Streamline diffusion parameter $\delta_{SD}$			
	0.05	0.1	0.3	0.5
$m_S(120\text{ s})$	17.11	17.05	16.90	16.79
$m_I(120\text{ s})$	1.29	1.29	1.24	1.20
$m_T(120\text{ s})$	18.41	18.34	18.14	17.99

$\delta_{SD} = 0.1$ ,  $\delta_{SD} = 0.3$ , and  $\delta_{SD} = 0.5$ , where a marginal decrease with increasing streamline diffusion can be seen. A range of values at the model end time is listed in Table 5.

#### 4.3. Computational results for the simplified model

In this section the simulations of the simplified model described in Section 3.9 are presented. First, the aggregate size  $\kappa$  is identified by simulating the amount of accumulated particles after 120 s, see Fig. 14. The shaded intervals denote the range for the experimental results for an inflow of  $m_{Fe} = 0.5$  mg,  $m_{Fe} = 1$  mg and  $m_{Fe} = 2$  mg iron, respectively, and a mean flux of  $Q = 3$  ml/min. Fig. 14 suggests an aggregate size around  $\kappa = 5$  (the curves lie in their corresponding experimental range near this value) and moreover also a dependence on the inflow concentration.

Since this dependence of the aggregate size  $\kappa$  on the inflow concentration is rather natural in the sense that larger aggregates appear for higher concentrations, one can use this idea to fit the values of Table 1. Choosing  $\kappa = 4.2, 4.7, 5.1$  for the inflow iron masses  $m_{Fe} = 0.5, 1.0, 2.0$  mg, respectively, the results plotted in Fig. 15 are obtained with the shaded regions showing the experimental values of Table 1. A quantitative comparison of the experimental and simulation values is shown in Table 6. The error of the simulation was assumed to be 5%



**Table 6**

Experimental and simulation results showing the retained percentage of iron mass for different fluxes and different injected suspension concentrations.

		Mean flux of peristaltic pump [ml/min]		
		3.0	6.0	11.0
Iron conc. [mg/ml]	1.0, exp.	21.4 ± 4.1	14.7 ± 5.3	12.6 ± 3.7
	1.0, sim.	22.7 ± 1.1	11.9 ± 0.6	6.8 ± 0.3
	2.0, exp.	27.6 ± 4.1	13.3 ± 2.8	8.7 ± 4.6
	2.0, sim.	28.2 ± 1.4	15.0 ± 0.7	8.6 ± 0.4
	4.0, exp.	35.4 ± 4.0	14.9 ± 4.3	8.2 ± 6.1
	4.0, sim.	32.8 ± 1.6	17.6 ± 0.9	10.0 ± 0.5

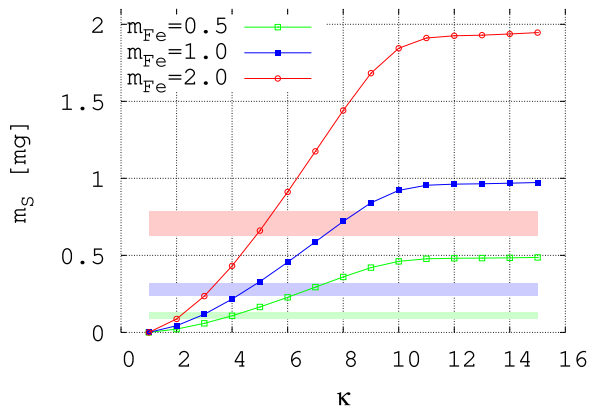


**Fig. 14.** Retained iron mass  $m_S$  after 120 s for different aggregate sizes and either an iron inflow  $m_{Fe}$  of 2 mg (red), 1 mg (blue), and 0.5 mg (green) at a fluid flow of 3 ml/min. For the simulations the time step was set to 0.5 s and the streamline diffusion parameter to  $\delta_{SD} = 0.3$ . The range for the experimental measurements results is shaded in the corresponding color.

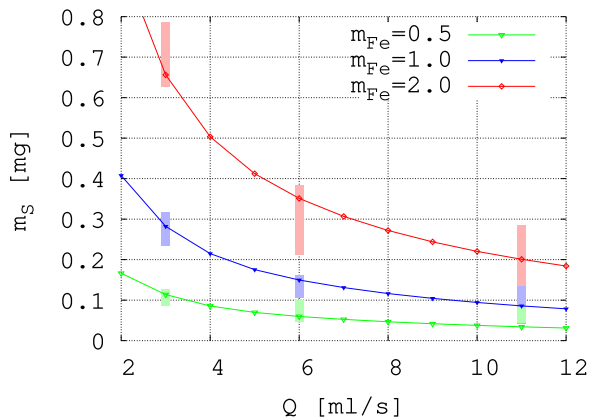


**Fig. 15.** Graphic representation of Table 6. Simulation of accumulated iron mass  $m_S$  (120 s) for different inflow masses and varying flux  $Q$ . Experimental values are shown as shaded regions.

because it is a result of spatial discretization error (approximately 3%), time discretization error (approximately 1%) and streamline diffusion modeling error (which was observed to be smaller than 1% earlier).

Finally, Fig. 16 shows a temporal sequence of the simulation for  $m_{Fe} = 2.0$  mg,  $Q = 3$  ml/min and  $\kappa = 5$ . Numerical parameters were set to  $\Delta t = 1$  s and  $\delta_{SD} = 0.3$ . In order to illustrate the spatial distribution in a representative way, the pipe is scaled in units of 10 cm in direction of  $x$  and in mm in direction of  $y$  and  $z$  in mm. The non-dimensional bulk concentration  $c$  and the surface concentration  $c_b$  are set to the same color scale, although  $c_b$  is measured in mm. It can be seen that the surface concentration  $c_b$  is mainly located close to the

pole shoe of the electromagnet. During the simulation time of 120 s the bulk concentration decreases rapidly whereas the surface concentration rises. This is in agreement with the quantitative results for the masses  $m_I$  and  $m_S$  in the interior respectively on the surface of the tube shown in Figs. 11–13.

## 5. Discussion

This contribution describes a basic Magnetic Drug Targeting experiment in distilled water together with a mathematical model and its numerical approximation. It turns out that the simulation results agree with the measurements within reasonable error bounds which are (for a larger part) due to errors in the measurements and (for a smaller part) due to simulation errors. This supports the correctness of the underlying mathematical model. We emphasize that an important modeling aspect was the assumption of the formation of SPION aggregates. Since the size of particle aggregates was not measured in the course of the experiment, this free parameter was fitted by using experimental data. Therefore, a very important issue in further research will be to eliminate this free parameter by determining experimentally the aggregate distribution occurring during the experiment. It is quite possible that the aggregate sizes depend on the precise circumstances of SPION injection, that this distribution may vary in time and space, and that this leads to a rather large range of results when repeating the experiment. In fact, this could easily be the source of the relatively large measurement errors from Table 1 which are calculated as the standard deviation of repeated measurements. In further experiments we will also use blood as fluid, since this will have an impact on fluid dynamics and possibly also on the magnetically induced formation of particle aggregates, which both could influence the targeting efficiency.

Finally, although the model used in this work was sufficient for simulating this experiment with acceptable accuracy, it could be improved in several regards. For example, it would be important to model fluid flow in the form of the Navier–Stokes equations instead of assuming a fixed parabolic flow profile. And, as already outlined in the previous paragraph, the SPION particles should be modeled as a structured population of aggregates of different sizes instead of a density of fixed-size aggregates. Finally, simulating the magnetic field and the drug targeting experiment within the same simulation environment would be profitable, because then variations of the magnetic field (for example by moving the electromagnet or modifying its strength) could be incorporated easily into simulations.

## CRedit authorship contribution statement

**Magdalena Reinelt:** Conceptualization, Methodology, Software, Visualization, Writing – original draft. **Johannes Ahlfs:** Experiments, Methodology, Writing – review & editing. **Rene Stein:** Experiments, Methodology, Writing – review & editing. **Christoph Alexiou:** Conceptualization, Methodology, Funding acquisition, Resources. **Eberhard Bänsch:** Conceptualization, Methodology, Writing – review & editing. **Ralf P. Friedrich:** Methodology, Writing – review & editing. **Stefan Lyer:** Conceptualization, Methodology, Visualization, Writing – original draft, Writing – review & editing. **Maria Neuss-Radu:** Conceptualization, Methodology, Writing – original draft, Writing – review & editing. **Nicolas Neuß:** Conceptualization, Methodology, Software, Writing – original draft, Writing – review & editing.

## Declaration of competing interest

Declare no conflict of interests.

## Data availability

Data will be made available on request.

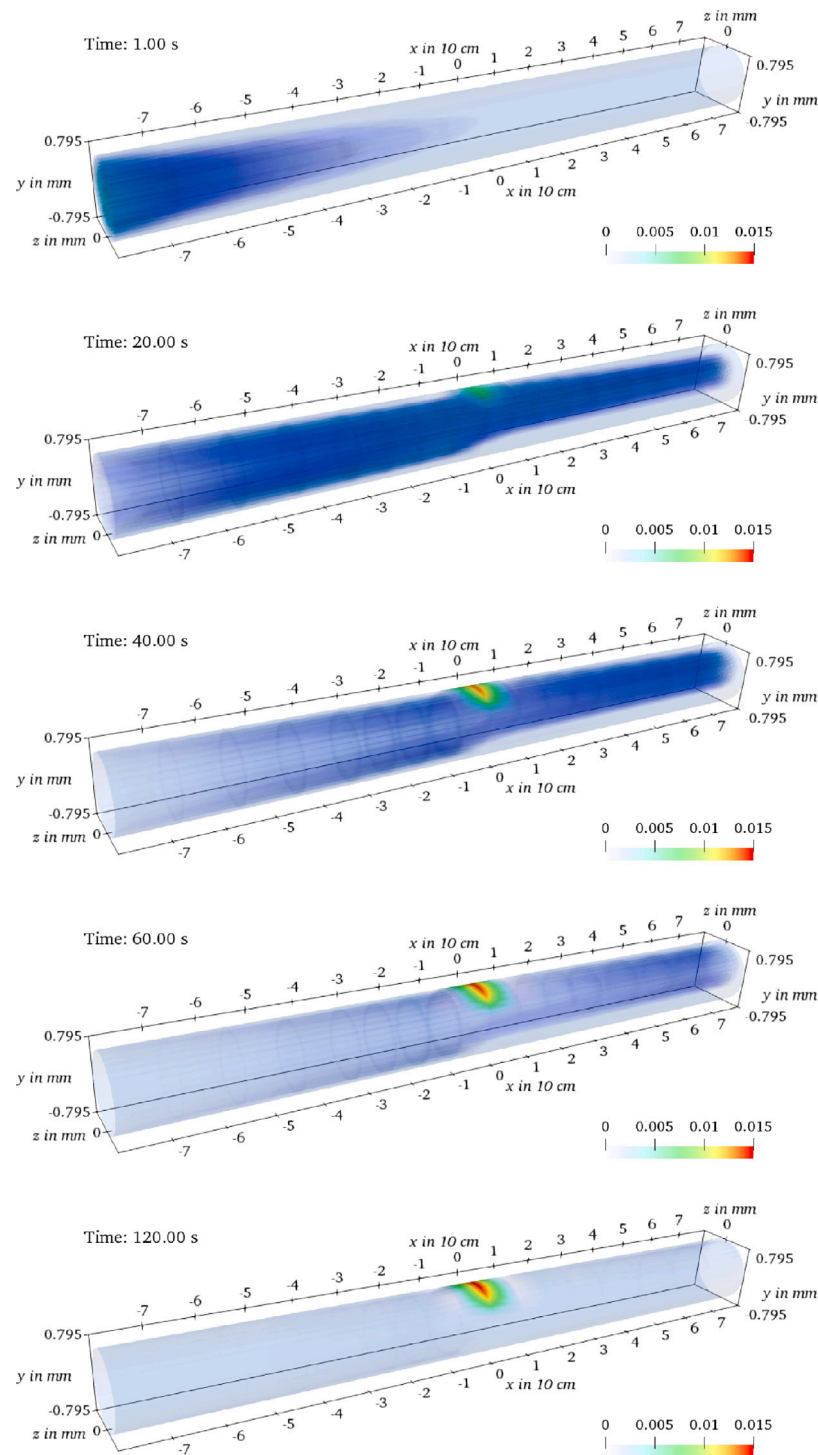


Fig. 16. Temporal evolution of  $c$  and  $c_b$  in the whole pipe. The mapping of each pipe is clinched, such that the scale of the  $x$ -axis is given in 10 cm, whereas the  $y$ - and  $z$ -axis are scaled in mm. The color scale is non dimensional corresponding to  $c$  and given in mm corresponding to  $c_b$ .

## Acknowledgments

The authors would like to thank the Manfred Roth-Stiftung, Fürth, Germany and the Forschungsstiftung Medizin am Universitätsklinikum Erlangen, Germany, for their support.

## References

- [1] A.K. Gupta, M. Gupta, Synthesis and surface engineering of iron oxide nanoparticles for biomedical applications, *Biomaterials* 26 (18) (2005) 3995–4021, <http://dx.doi.org/10.1016/j.biomaterials.2004.10.012>, URL <https://www.sciencedirect.com/science/article/pii/S0142961204009317>.
- [2] R. Reszka, P. Beck, I. Fichtner, M. Hentschel, J. Richter, J. Kreuter, Body distribution of free, liposomal and nanoparticle-associated mitoxantrone in B16-melanoma-bearing mice, *J. Pharmacol. Exp. Ther.* 280 (1) (1997) 232–237.
- [3] H. Unterwiesing, R. Tietze, C. Janko, J. Zaloga, S. Lyrer, S. Dürr, N. Taccardi, O.-M. Goudouri, A. Hoppe, D. Eberbeck, D.W. Schubert, A.R. Boccaccini, C. Alexiou, Development and characterization of magnetic iron oxide nanoparticles with a cisplatin-bearing polymer coating for targeted drug delivery, *Int. J. Nanomedicine* 9 (2014) 3659–3676, <http://dx.doi.org/10.2147/IJN.S63433>.
- [4] R. Tietze, S. Lyrer, S. Dürr, T. Struffert, T. Engelhorn, M. Schwarz, E. Eckert, T. Goen, S. Vasylyev, W. Peukert, F. Wiekhorst, L. Trahms, A. Dorfner, C.

- Alexiou, Efficient drug-delivery using magnetic nanoparticles - biodistribution and therapeutic effects in tumour bearing rabbits, *Nanomed.-Nanotechnol. Biol. Med.* 9 (2013) 961–971, <http://dx.doi.org/10.1016/j.nano.2013.05.001>.
- [5] K. Gitter, S. Odenbach, Quantitative targeting maps based on experimental investigations for a branched tube model in magnetic drug targeting, *J. Magn. Magn. Mater.* 323 (23) (2011) 3038–3042, <http://dx.doi.org/10.1016/j.jmmm.2011.06.055>.
  - [6] E.P. Furlani, K.C. Ng, Analytical model of magnetic nanoparticle transport and capture in the microvasculature, *Phys. Rev. E* 73 (2006) 061919, <http://dx.doi.org/10.1103/PhysRevE.73.061919>, URL <https://link.aps.org/doi/10.1103/PhysRevE.73.061919>.
  - [7] M.C. Lindemann, T. Luttkie, N. Nottrodt, T. Schmitz-Rode, I. Slabu, FEM based simulation of magnetic drug targeting in a multibranched vessel model, *Comput. Methods Programs Biomed.* 210 (2021) 106354, <http://dx.doi.org/10.1016/j.cmpb.2021.106354>, URL <https://www.sciencedirect.com/science/article/pii/S0169260721004284>.
  - [8] A.D. Grief, G. Richardson, Mathematical modelling of magnetically targeted drug delivery, *J. Magn. Magn. Mater.* 293 (1) (2005) 455–463, <http://dx.doi.org/10.1016/j.jmmm.2005.02.040>, URL <https://www.sciencedirect.com/science/article/pii/S0304885305002015>, Proceedings of the Fifth International Conference on Scientific and Clinical Applications of Magnetic Carriers.
  - [9] S.A. Khashan, E. Elhajjar, Y. Haik, CFD simulation of the magnetophoretic separation in a microchannel, *J. Magn. Magn. Mater.* 323 (23) (2011) 2960–2967, <http://dx.doi.org/10.1016/j.jmmm.2011.06.001>, URL <https://www.sciencedirect.com/science/article/pii/S0304885311003337>.
  - [10] K. Gitter, S. Odenbach, Investigations on a branched tube model in magnetic drug targeting—Systematic measurements and simulation, *IEEE Trans. Magn.* 49 (1) (2013) 343–348, <http://dx.doi.org/10.1109/TMAG.2012.2224324>.
  - [11] A. Nacev, C. Beni, O. Bruno, B. Shapiro, The behaviors of ferromagnetic nanoparticles in and around blood vessels under applied magnetic fields, *J. Magn. Magn. Mater.* 323 (6) (2011) 651–668, <http://dx.doi.org/10.1016/j.jmmm.2010.09.008>.
  - [12] A. Daddi-Moussa-Ider, S. Goh, B. Liebchen, C. Hoell, A.J.T.M. Mathijssen, F. Guzmán-Lastra, C. Scholz, A.M. Menzel, H. Löwen, Membrane penetration and trapping of an active particle, *J. Chem. Phys.* 150 (6) (2019) 064906, <http://dx.doi.org/10.1063/1.5080807>, [arXiv:https://doi.org/10.1063/1.5080807](https://doi.org/10.1063/1.5080807).
  - [13] S. Majee, G.C. Shit, Modeling and simulation of blood flow with magnetic nanoparticles as carrier for targeted drug delivery in the stenosed artery, *Eur. J. Mech. B Fluids* 83 (2020) 42–57, <http://dx.doi.org/10.1016/j.euromechflu.2020.04.004>.
  - [14] S. Shaw, G. Shit, D. Tripathi, Impact of drug carrier shape, size, porosity and blood rheology on magnetic nanoparticle-based drug delivery in a microvessel, *Colloids Surf. A* 639 (2022) 128370, <http://dx.doi.org/10.1016/j.colsurfa.2022.128370>, URL <https://www.sciencedirect.com/science/article/pii/S0927775722001248>.
  - [15] K. Kakavand, N. Koosha, K. Fathi, S. Aminian, Numerical investigation of capture efficiency of carrier particles in a Y-shaped vessel considering particle-particle interaction and non-Newtonian behavior, *J. Drug Deliv. Sci. Technol.* 67 (2022) 102997, <http://dx.doi.org/10.1016/j.jddst.2021.102997>, URL <https://www.sciencedirect.com/science/article/pii/S1773224721006778>.
  - [16] D. Himmelsbach, M. Neuss-Radu, N. Neuß, Mathematical modelling and analysis of nanoparticle gradients induced by magnetic fields, *J. Math. Anal. Appl.* 461 (2) (2018) 1544–1560, <http://dx.doi.org/10.1016/j.jmaa.2017.12.026>, URL <http://www.sciencedirect.com/science/article/pii/S0022247X17311046>.
  - [17] G. De Las Cuevas, J. Faraudo, J. Camacho, Low-gradient magnetophoresis through field-induced reversible aggregation, *J. Phys. Chem. C* 112 (4) (2008) 945–950, <http://dx.doi.org/10.1021/jp0755286>, [arXiv:https://doi.org/10.1021/jp0755286](https://doi.org/10.1021/jp0755286).
  - [18] M. Mühlberger, H. Unterwiesing, J. Band, C. Lehmann, L. Heger, D. Dudziak, C. Alexiou, G. Lee, C. Janko, Loading of primary human T lymphocytes with citrate-coated superparamagnetic iron oxide nanoparticles does not impair their activation after polyclonal stimulation, *Cells* 9 (2) (2020) <http://dx.doi.org/10.3390/cells9020342>, URL <https://www.mdpi.com/2073-4409/9/2/342>.
  - [19] S. Dürr, R. Tietze, S. Lyer, C. Janko, E. Schreiber, J. Mann, R. Turcu, K. Gitter, S. Odenbach, S. Vasylyev, M. Herrmann, W. Peukert, C. Alexiou, A high field gradient magnet for magnetic drug targeting, *Magnetohydrodynamics* 49 (2013) 552–559, <http://dx.doi.org/10.22364/mhd.49.3-4.56>.
  - [20] C. Alexiou, D. Diehl, P. Henninger, H. Iro, R. Rockelein, W. Schmidt, H. Weber, A high field gradient magnet for magnetic drug targeting, *IEEE Trans. Appl. Supercond.* 16 (2006) 1527–1530, <http://dx.doi.org/10.1109/TASC.2005.864457>.
  - [21] C.F. Driscoll, R.M. Morris, A.E. Senyei, K.J. Widder, G.S. Heller, Magnetic targeting of microspheres in blood flow, *Microvasc. Res.* 27 (3) (1984) 353–369, [http://dx.doi.org/10.1016/0026-2862\(84\)90065-7](http://dx.doi.org/10.1016/0026-2862(84)90065-7).
  - [22] L. Vaidman, Torque and force on a magnetic dipole, *Amer. J. Phys.* 58 (10) (1990) 978–983, <http://dx.doi.org/10.1119/1.16260>.
  - [23] J. Heintze, *Lehrbuch zur Experimentalphysik: Band 3: Elektrizität Und Magnetismus*, first Auflage ed., in: *Lehrbuch*, Springer Spektrum, Berlin and Heidelberg, 2016, <http://dx.doi.org/10.1007/978-3-662-48451-7>.
  - [24] J.D. Jackson, *Classical Electrodynamics*, second ed., Wiley, New York, NY, 1975, URL <https://cds.cern.ch/record/100964>.
  - [25] G.K. Batchelor, *An Introduction to Fluid Dynamics*, in: *Cambridge Mathematical Library*, Cambridge University Press, 2000, <http://dx.doi.org/10.1017/CBO9780511800955>.
  - [26] C.T. Yavuz, J.T. Mayo, W.W. Yu, A. Prakash, J.C. Falkner, S. Yean, L. Cong, H.J. Shipley, A. Kan, M. Tomson, D. Natelson, V.L. Colvin, Low-field magnetic separation of monodisperse Fe<sub>3</sub>O<sub>4</sub> nanocrystals, *Science* 314 (5801) (2006) 964–967, <http://dx.doi.org/10.1126/science.1131475>.
  - [27] N. Wise, T. Grob, K. Morten, I. Thompson, S. Sheard, Magnetophoretic velocities of superparamagnetic particles, agglomerates and complexes, *J. Magn. Magn. Mater.* 384 (2015) 328–334, <http://dx.doi.org/10.1016/j.jmmm.2015.02.031>.
  - [28] A. Einstein, Über die von der molekularkinetischen theorie der wärme geforderte bewegung von in ruhenden flüssigkeiten suspendierten teilchen, *Ann. Phys.* 322 (1905) 549–560.
  - [29] E. Blums, Some new problems of complex thermomagnetic and diffusion-driven convection in magnetic colloids, *J. Magn. Magn. Mater.* 149 (1–2) (1995) 111–115, [http://dx.doi.org/10.1016/0304-8853\(95\)00350-9](http://dx.doi.org/10.1016/0304-8853(95)00350-9).
  - [30] A. Nacev, A. Komae, A. Sarwar, R. Probst, S.H. Kim, M. Emmert-Buck, B. Shapiro, Towards control of magnetic fluids in patients: Directing therapeutic nanoparticles to disease locations, *IEEE Control Syst.* 32 (3) (2012) 32–74, <http://dx.doi.org/10.1109/MCS.2012.2189052>.
  - [31] S. Odenbach, M. Liu, Invalidation of the kelvin force in ferrofluids, *Phys. Rev. Lett.* 86 (2) (2001) 328–331, <http://dx.doi.org/10.1103/physrevlett.86.328>.
  - [32] FEMLISP website, 2010–2023, <http://www.femlisp.org>.
  - [33] N. Neuß, *Femlisp – A Multi-Purpose Tool for Solving Partial Differential Equations*, Tech. Rep., Interdisciplinary Center for Scientific Computing (IWR), Heidelberg University, 2003.
  - [34] Y. Saad, *Iterative Methods for Sparse Linear Systems*, second ed., Society for Industrial and Applied Mathematics, Philadelphia, PA, 2003, p. xviii+528.